Journal of Metals, Materials and Minerals, Vol. 30, No. 3, pp. 38-45, 2020

Incorporation of Fe and Cu for antibacterial performance enhancement of Fe-Cu-ZnO nanocomposites synthesized by a facile chemical precipitation

Sucheewan KROBTHONG and Sutthipoj WONGRERKDEE*

Department of Physics, Faculty of Liberal Arts and Science, Kasetsart University Kamphaeng Saen Campus, Nakhon Pathom 73140, Thailand

***Corresponding author e-mail:** sutthipoj.s@ku.ac.th

Received date:
18 November 2019
Revised date:
13 June 2020
Accepted date:
17 June 2020

Keywords:
ZnO; iron
Copper
Antibacterial
Performance

Abstract

Fe-Cu-ZnO nanocomposites were synthesized using simple chemical precipitation under a violent stirring condition, and characterized by dynamic light scattering, ultraviolet-visible spectroscopy, scanning electron microscopy, X-ray diffractometry, Raman spectroscopy, and vibrating sample magnetometer. The particle size distribution is observed not only a large size of 100 nm to 2 μm, but also a small size of 0.4-5.0 nm. The absorbance peaks of the nanocomposites exhibit a small blue shift in comparison with ZnO. Surface defects are explored in the nanocomposites including irregular shapes, rough surfaces, and aggregation. The nanocomposites and ZnO have similar hexagonal wurtzite structures. However, the nanocomposites have more crystal defects than ZnO due to $ZnFe_2O_4$ formation. Although the presence of zinc ferrite ($ZnFe_2O_4$) is also detected, magnetic hysteresis is disappeared because of poor $ZnFe_2O_4$ distribution and critical size effects. In antibacterial test, the nanocomposites were applied to inhibit the growth of *Xanthomonas campestris*, *Pseudomonas aeruginosa*, and *Pseudomonas fluorescens*. It is found that antibacterial performance is enhanced relating to surface and crystal defects. These defects are possible to increase interfacial contacts and accelerate antibacterial activities for the antibacterial enhancement. Therefore, the Fe-Cu-ZnO nanocomposites are alternative potential material appropriately for bacterial inhibition application.

1. Introduction

Nowadays, nanotechnology has been utilized with several fields. One of applied nanotechnology is antimicrobial agents such as bacteria, viruses, and other pathogenic microorganisms [1,2]. Since, nanotechnology able to improve antimicrobial performance in many parts. For instances, nanostructures of material as well as the nanoparticle form can well penetrate the bacterial cell wall, high surface-to-volume ratios can improve interfacial contacts with outer surfaces of cell walls, and so on. Varieties of nanomaterials such as ZnO, Fe_2O_3, TiO_2, Ag_2O, CaO, MgO, and CuO have been extensively studied as efficient antibacterial agents [3,4]. Among these nanomaterials, ZnO is an interesting material because it has appropriate properties, e.g. chemical stability, biological safety, effective low cost, non-toxicity, possible large-scale production, etc. [5,6]. The antibacterial properties of ZnO nanoparticles (NPs) are possibly improved by modification of particle sizes and surface morphologies. ZnO-based antibacterial performance has been demonstrated in varieties of bacteria that cause disease in plants, animals, and humans. For examples, the inhibition rates of *Bacillus thuringiensis israelensis* (*Bti*) and *Escherichia coli* (*E. coli*) were investigated using ZnO tetrapods [7]. It was found that the inhibition rates increased as a function of ZnO tetrapod concentration, and both strains were completely inhibited at the concentration of 0.75 $mg \cdot ml^{-1}$ [7]. The bactericidal efficiency of rare earth element (REE) doped ZnO nanoparticles was also investigated against *Bacillus subtilis* (*B. subtilis*), *Staphylococcus aureus* (*S. aureus*), *Proteus mirabilis* (*P. mirabilis*), and *Salmonella typhi* (*S. typhi*) [8,9]. The REE (Ag, Au, Pd) influenced on structural and optical properties of ZnO which resulted in enhanced antibacterial performance. Most of metal-doped ZnO materials exhibited high antibacterial activity with very low minimum inhibitory concentration (MIC) values. In addition, the materials showed the possibility of bacterial inhibition for both Gram-positive and Gram-negative [10].

In this research, ZnO and Fe-Cu-ZnO nanocomposites were synthesized by simple chemical precipitation method from conventional starting materials of Zn $(NO_3)_2 \cdot 6H_2O$ and $NaHCO_3$. Iron (Fe) and copper (Cu) were mixed with the starting materials to synthesize Fe-Cu-ZnO nanocomposites. The synthesized materials have been characterized using several techniques. Then, it was applied as antibacterial material to inhibit the growth of *Xanthomonas campestris* (*X. campestris*), *Pseudomonas fluorescens* (*P. fluorescens*), and *Pseudomonas aeruginosa* (*P. aeruginosa*). The investigation purposes to demonstrate performance of ZnO-based nanocomposite materials for antibacterial application. It is expected that material characteristics of the nanocomposite formation with additional metals (Fe and Cu) could be modified such as shapes, roughness, aggregation, etc. [10]. It is well-known that the high surface-to-volume ratios, effecting from

DOI: 10.14456/jmmm.2020.36

nanostructures or rough surfaces, can provide interfacial contacts between materials and bacterial cell walls. Moreover, crystal defects could occur at the same time which act as interaction centers for accelerating antibacterial mechanism. These effects could possibly achieve the enhancement of antibacterial performance.

2. Experimental

ZnO was synthesized from starting materials of $Zn(NO_3)_2{\cdot}6H_2O$ and $NaHCO_3$. These starting materials were separately prepared. Firstly, a concentration of 0.1 M $Zn(NO_3)_2{\cdot}6H_2O$ was dissolved in distilled water to form the zinc nitrate solution with stirring at room temperature for 1 h. Another one, a concentration of 0.2 M $NaHCO_3$ was dissolved in distilled water to form $NaHCO_3$ solution with stirring and heating at 60°C for 1 h. For precipitation process, the zinc nitrate solution was added, drop by drop, to the $NaHCO_3$ solution under stirring and heating at 60°C for 1 h. Then, the mixtures were adjusted pH to 9.0 by dropping NaOH solution with continuous stirring for 1 h. After cooling down to room temperature, the adjusted mixtures were filtered by filtering paper to obtain white-gel products. The products were heated at 120°C for 1 h, and then crushed before stocking in a brown bottle. For Fe-Cu-ZnO nanocomposite synthesis, $Fe(NO_3)_3{\cdot}9H_2O$, $Cu(NO_3)_2{\cdot}3H_2O$, and $Zn(NO_3)_2{\cdot}6H_2O$ were mixed and dissolved in distilled water with stirring at room temperature for 1 h. Molecular ratios of starting materials were calculated, and all materials were mixed in same beaker. $Fe(NO_3)_3{\cdot}9H_2O$:$Cu(NO_3)_2{\cdot}3H_2O$:$Zn(NO_3)_2{\cdot}6H_2O$ molar ratios were varied as 5:15:80, 10:10:80, 15:5:80, and called as Fe5Cu15, Fe10Cu10, Fe15Cu5, respectively. Then, the precipitation process was carried out to form Fe-Cu-ZnO nanocomposites similarly as the previous description of ZnO. All synthesized materials (ZnO and the nanocomposites) were characterized using several techniques. Particle size distribution was measured by using dynamic light scattering (DLS) technique. Absorbance was measured by using ultraviolet-visible (UV-Vis) spectroscopy. Morphology was examined by using scanning electron microscopy (SEM). The crystal structure was investigated by using X-ray diffractometry (XRD). Vibration characteristics were observed by using Raman spectroscopy. The magnetic property was observed by using a vibrating sample magnetometer (VSM) measurement. After the characterization, the synthesized materials were examined for investigating antibacterial activity.

The antibacterial activity of the synthesized materials was tested with representative pathogens (*X. campestris*, *P. fluorescens*, and *P. aeruginosa*) in a sterilized plate by broth microdilution assay with minor modifications [11]. In the details, the stock of each bacterial strain was diluted with medium culture to obtain OD600 between 0.07-0.10 bacterial suspension solution. 100 µl of the suspension solution was mixed with 10 µl of each the synthesized materials in dose-dependent manners (0-50000 ppm). The sterile water and Penicillin was used as negative control and positive control, respectively. The plates were incubated at 37ºC under shaking conditions (200 rpm). After 16 h, the bacterial growth was monitored by measurement of the optical density at 600 nm, and the bacterial inhibition was calculated.

3. Results and discussion

Particle size distribution in Figure 1 shows various ranges of particle size including nanostructures, submicrostructures, and microstructures. The particle sizes around 100 nm to 2 µm are the most observation. However, detected distribution also exists the small particle sizes in a range of 0.4-5.0 nm. It could indicate that the Fe-Cu-ZnO nanocomposites are free-formed during the chemical reaction and precipitation. This formation is a well-known behavior in natural reaction for the chemical precipitation process due to an uncontrollable growth direction. For absorbance result in Figure 2, the absorbance peak of ZnO locating around 402 nm is observed, whereas the nanocomposites exhibit a small blue shift. It is found that there is a direct correlation between amount of blue shift and Cu-content. So, the result also imply that Cu majorly cause the blue shift effect associating with surface plasmon resonance or poor crystallinity due to surface defects [12]. As mentioned, it is consistent with the change of morphology as shown in Figure 3. Morphological image of ZnO shows multi-particle sizes with regular shapes including hexagons and spheres. Meanwhile, the Fe-Cu-ZnO nanocomposites explore irregular shapes which cause the increasing surface defects. Moreover, cluster formation of popcorn-like structures is also observed signifying the aggregation behavior of numerous nanoparticles. The change of morphology can effectively provide high surface-to-volume ratios [13].

XRD spectra as shown in Figure 4 can be interpreted that crystal structures are hexagonal wurtzite for ZnO and the nanocomposites according to the JCPDS card no. 36-1451 [14,15]. However, the peak width and intensity are differences between ZnO and the nanocomposites. The narrow peak and high intensity of ZnO refer to the large crystal size and high crystallinity, respectively. On the other hand, the broad peak and low intensity are detected in the nanocomposites. This means that the nanocomposites have small crystal size and low crystallinity. These effects indicate that the incorporation of Fe and Cu can affect to crystallization of the nanocomposites. In analyzing, metal substitution is not occurred according to no observation of XRD diffraction shifts. Meanwhile, three extra peaks at 2θ around 29.94°, 35.28°, and 42.86° are observed for the $Fe_{15}Cu_5$ sample [16]. These peaks possibly refer to the zinc ferrite ($ZnFe_2O_4$) formation for higher Fe-content [17,18]. In addition, this formation also occurs with other lower Fe-content samples as can be seen from the baseline shifting between the peak (002) and (101), whereas the effect of Cu-content shows non-obvious significance to change the nanocomposite crystal. For crystal characteristic growth analysis, lattice parameters were calculated and listed in Table 1 using the Equation (1)-(3) [19,20].

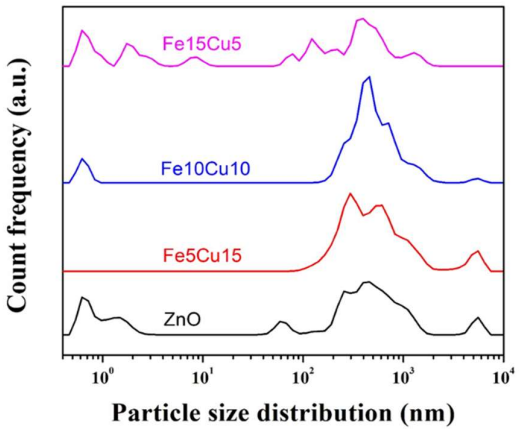

Figure 1. Particle size distribution of ZnO and Fe-Cu-ZnO nanocomposites.

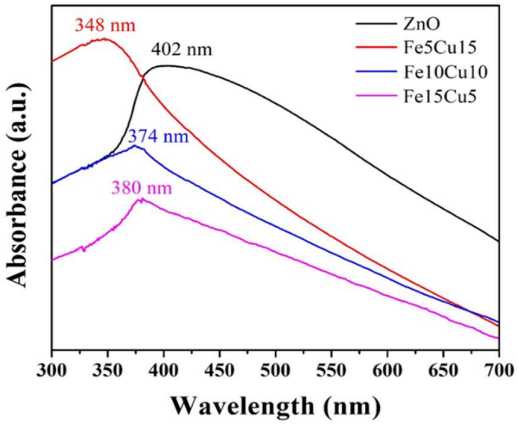

Figure 2. Absorbance spectra of ZnO and Fe-Cu-ZnO nanocomposites.

Table 1. Lattice constants and interplanar spacing.

Samples	a (Å)	c (Å)	d_{100} (Å)	d_{002} (Å)	d_{101} (Å)
ZnO	3.254	5.212	2.520	2.331	2.217
Fe5Cu15	3.254	5.199	2.520	2.325	2.219
Fe10Cu10	3.254	5.214	2.520	2.332	2.218
Fe15Cu5	3.252	5.207	2.519	2.329	2.217

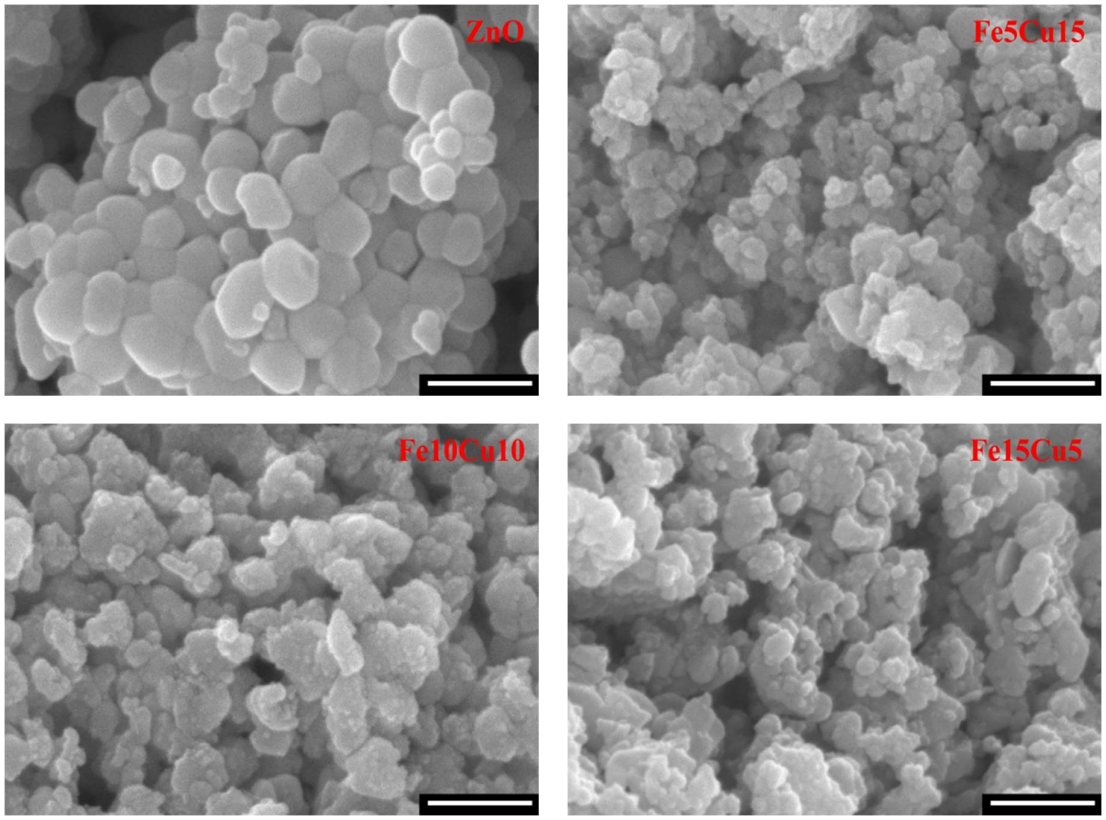

Figure 3. Morphological images of ZnO and Fe-Cu-ZnO nanocomposites (the scale bar length is 500 nm).

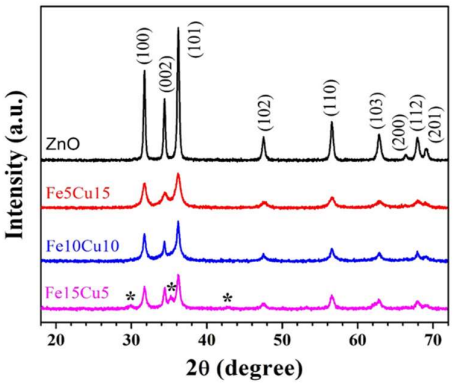

Figure 4. XRD patterns of ZnO and Fe-Cu-ZnO nanocomposites.

$$a = \frac{\lambda}{\sqrt{3}\sin\theta} \quad (1)$$

$$c = \frac{\lambda}{\sin\theta} \quad (2)$$

$$\frac{1}{d_{hkl}^2} = \frac{4}{3}\left(\frac{h^2+hk+k^2}{a^2}\right) + \frac{l^2}{c^2} \quad (3)$$

The lattice constants "a" and "c" are calculated from the (100) and (002) planes, respectively. The d_{hkl} is interplanar spacing correlated to miller indices of h, k, and l. The λ and θ are the wavelengths of X-ray source (1.5406 Å) and diffraction angle, respectively. The calculated lattice constants (a and c) show little change for all synthesized materials [18], confirmed by the similar c/a ratio around 1.60 as equal as the ideal and standard JCPDs values. This ratio can be described that the crystal growth mechanism in (002) plane is faster than (100) plane. For interplanar spacing analysis, the three major peaks of (100), (002), and (101) planes show also little differences. It seems that the crystal growth mechanism of all nanocomposites is similar to ZnO. These results mean that there is no effect of metals on crystal structures confirming no substitution. Although the Fe^{3+} ions and Cu^{2+} ions have lower ionic radius than Zn^{2+} ions [17,21], the substitution has no occurrence in this case. This effect may be due to violent vibration during precipitation method, normal atmospheric precipitation, or comparative higher concentration of zinc ions. Then, preferred orientation and crystal size (D) and were calculated using the Equation (4)-(5) [20,22], and listed in Table 2.

$$T_c = \frac{\frac{I_{(hkl)}}{I_{0(hkl)}}}{\frac{1}{N}\Sigma\left(\frac{I_{(hkl)}}{I_{0(hkl)}}\right)} \quad (4)$$

$$D = \frac{k\lambda}{\beta\cos\theta} \quad (5)$$

Table 2. Texture coefficient and crystal size.

Samples	$T_{c(100)}$	$T_{c(002)}$	$T_{c(101)}$	D (nm)
ZnO	1.113	0.955	0.932	26.752
Fe5Cu15	1.261	0.797	0.942	10.866
Fe10Cu10	1.168	0.915	0.917	19.625
Fe15Cu5	0.965	1.178	0.856	17.522

T_c is the texture coefficient, $I_{(hkl)}$ is the measured intensity of preferred orientation plane, $I_{0(hkl)}$ is the standard JCPDs intensity of preferred orientation plane, N is the number of considered planes, k is the constant (0.89), and β is the full-width at half-maximum (FWHM). Generally, $T_{c(100)}$ and $T_{c(002)}$ refer to growth direction in a-axis and c-axis, respectively, while the $T_{c(101)}$ means growth direction between both of those axes. In calculated T_c results of ZnO, there are not much different values for the three major planes. All T_c values are closed to 1, referring to the random growth direction [23]. Therefore, spherical growth can be assumed corresponding to the morphological images. For the nanocomposites, all T_c values have obvious changing. The $T_{c(100)}$ shows maximal value than $T_{c(002)}$ and $T_{c(101)}$ for the Fe5Cu15 and Fe10Cu10 samples, while the $T_{c(002)}$ value is the maximum for the Fe15Cu5 sample. In crystal size analysis, the nanocomposites have smaller crystal size than ZnO [17]. It can be implied that crystal growth mechanism is intercepted by metals. It is possible that metals might react with surrounding oxygen and gradual decreases oxygen sources during chemical precipitation process. This reaction effectively decreases crystal sizes, and increases crystal defects such as grain boundary density or metal interstitial [24]. Furthermore, surface defects could also be formed due to the reaction according to the rough morphological observation [25,26].

Raman spectra were measured as shown in Figure 5, and analyzed from the group theory of vibration modes. The ZnO shows a strong peak at 436 cm^{-1} assigned to E_{2H} mode which is the characteristic peak of Raman active mode. The peak around 330 cm^{-1} presents the boundary phonon E_{2H}-E_{2L} mode. The weak peaks at 383 cm^{-1} and 583 cm^{-1} correspond to the transverse optical A_{1T} mode and the E_{1L} mode, respectively. These fundamental Raman modes indicate the hexagonal wurtzite crystal phase of ZnO [27]. In the nanocomposite cases, the change of these peaks is observed. The major peak E_{2H} mode slightly shifts to the higher Raman shift (Figure 5(b)), indicating stronger vibration of ZnO-O because of lower binding energy. This effect could be a result of crystal defects which is caused by imperfect

crystal structures in agreement with the XRD results. Moreover, the apparent peak around 648 cm^{-1} is detected which also confirms the presence of defects such as oxygen vacancy (V_O), zinc interstitial (I_{Zn}), structural impurity, etc. [20].

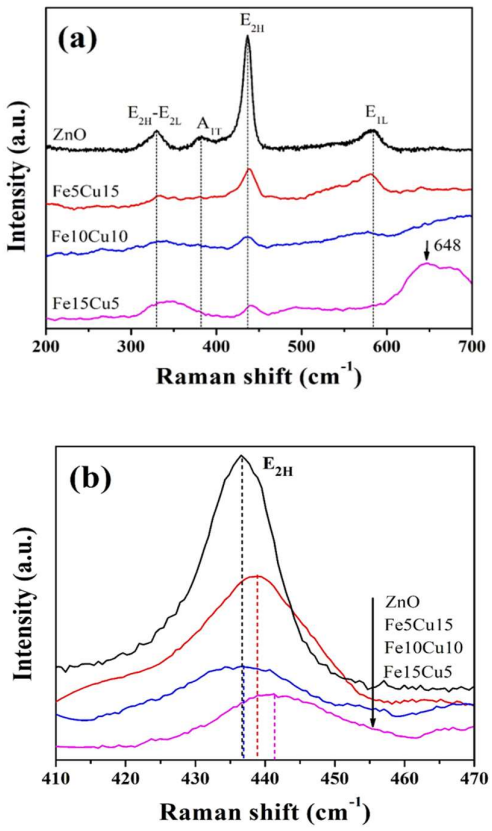

Figure 5. Raman shift of (a) ZnO and Fe-Cu-ZnO nanocomposites, (b) E2H mode.

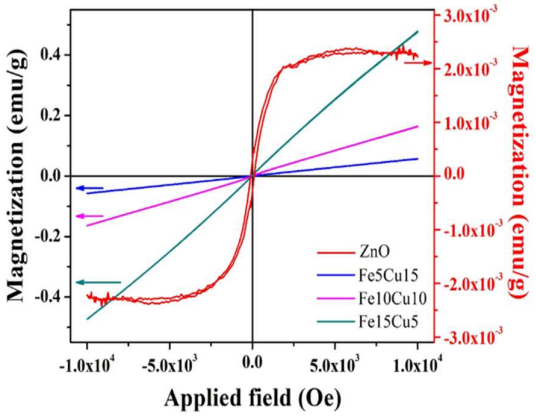

Figure 6. Magnetic hysteresis (M-H) curves of ZnO and Fe-Cu-ZnO nanocomposites.

Figure 6 shows the magnetic hysteresis (M-H) curves of ZnO and the nanocomposites. The pure ZnO presents ferromagnetic behavior with coercive field of 10^4 Oe and saturated magnetization of 2.3×10^{-3} emu·g^{-1} [21]. However, the magnetic property changes to paramagnetic behavior for the nanocomposites [21]. The magnetic property of the nanocomposites is different from previous reports [20], and it is inconsistent with the presence of $ZnFe_2O_4$ in XRD result. The paramagnetic behavior of the nanocomposites could be described in either of two effects. The first one is the poor distribution of $ZnFe_2O_4$ in the nanocomposites. The poor distribution causes the scanty connectivity of $ZnFe_2O_4$ formation which results in a very low density of magnetic domain. The second one is the critical size effects where the nanocomposites have smaller crystal sizes than the critical sizes [28] as well-known as the decreasing magnetic domain. The small crystal sizes could affect high cationic disorder and the unstable crystal phase at the same time [29]. So that coercivity disappears because it has no residual magnetic flux density, even though the higher magnetic moment of Fe^{2+} ions can comparatively gain stronger magnetization at the same applied field [30].

For analyzing antibacterial performance, bacterial activities of *X. campestris*, *P. aeruginosa*, and *P. fluorescens* were monitored from the optical density at 600 nm [29]. Then, the antibacterial performance was evaluated in term of inhibition rate, calculated from the Equation (6) [7];

$$Inhibition\ rate\ (\%) = \left(1 - \frac{OD_{sample}}{OD_{control}}\right) \times 100\% \qquad (6)$$

OD_{sample} and $OD_{control}$ are the optical density of the sample and control condition, respectively. The calculated inhibition rate was plotted as shown in Figure 7, the vertical dash line means the first approach to 100% inhibition for each pathogen. For *X. campestris* test as shown in Figure 7(a), the nanocomposites explore a better inhibition rate than ZnO. *X. campestris* is inhibited absolutely by the nanocomposites at inhibitor dosage of 1000-5000 ppm, while pure ZnO is required high dosage up to 10000 ppm. Figure 7(b) reveals that the inhibition rate of *P. aeruginosa* approaches 100% at 10000-50000 ppm. From the Figure 7(c), inhibition rate of *P. fluorescens* present similar linear trends at the inhibitor dosage of 500-5000 ppm for all synthesized materials, and this strain is inhibited completely at 5000-10000 ppm. Among these strains, *P. aeruginosa* has the ability to resist inhibiting materials rather than other strains. Since, the *P. aeruginosa* can survive and thrive under various conditions such as wide temperature range, different nutrient sources, pressured environment, etc. [32,33]. However, it can be inhibited using the nano-composites accordingly. For performance evaluation of antibacterial material, MIC values were listed in Table 3. It demonstrates that the Fe10Cu10 sample is the most appropriate inhibitor for all representative bacteria. Note that if the consideration is performed for

each bacteria inhibition, other samples of the nanocomposites are also able to be appropriate inhibitor. Thus, these results can be interpreted that antibacterial performance is enhanced successfully using Fe-Cu-ZnO nanocomposites. The enhancement is caused by the appropriate characteristic formation; especially the defects including surface and crystal defects, of the nanocomposites. It is possible that these defects can increase interfacial contacts between nanocomposite surfaces and bacterial cell walls [34], and accelerate antibacterial activities for breaking bacterial cell walls with high rates [35]. Therefore, the defects of Fe-Cu-ZnO nanocomposites can be considered as an effective material for bacterial inhibition.

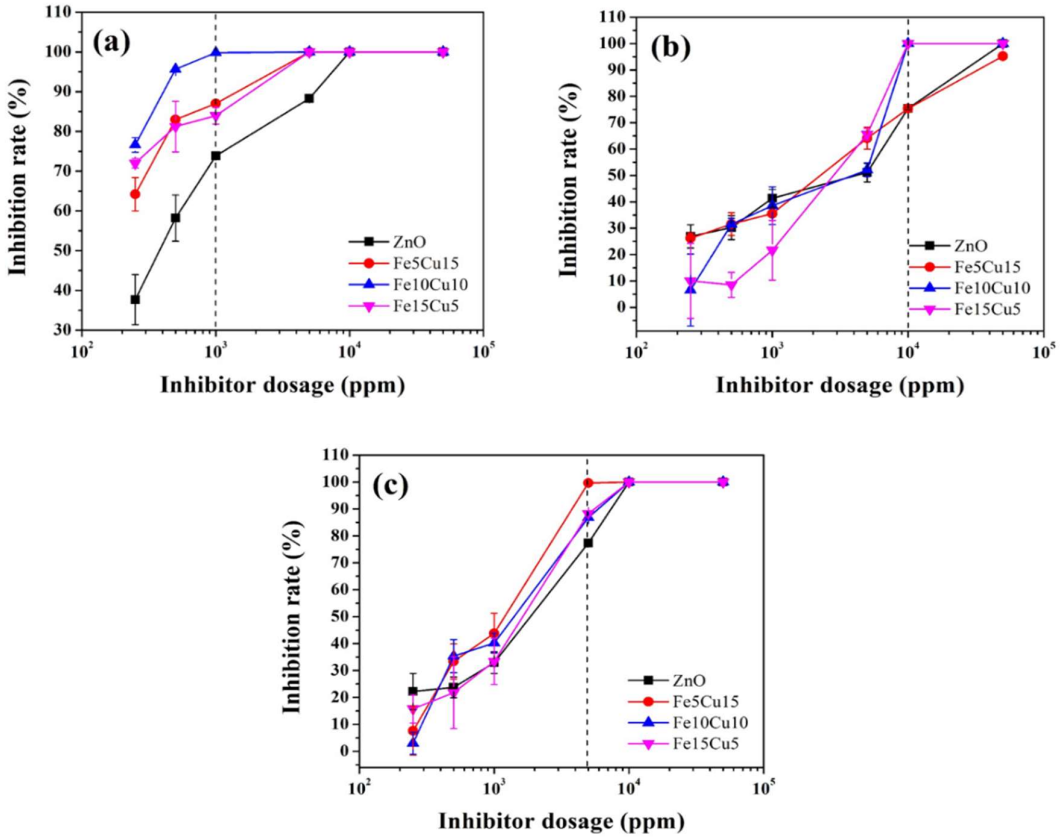

Figure 7. Inhibition rate of antibacterial test of ZnO and Fe-Cu-ZnO nanocomposites for (a) *X. campestris,* (b) *P. aeruginosa*, and (c) *P. fluorescens*

Table 3. Summary of MIC values (in ppm) for complete inhibition.

Samples	*X. campestris*	*P. aeruginosa*	*P. fluorescens*
ZnO	10000	50000	10000
Fe5Cu15	5000	-	5000
Fe10Cu10	1000	10000	10000
Fe15Cu5	5000	10000	10000

4. Conclusions

Fe-Cu-ZnO nanocomposites were synthesized using simple chemical precipitation under a violent stirring condition and characterized using several techniques. Addition of the metals is purposed to increase defects in the nanocomposites. Then, antibacterial performance of the nanocomposites was investigated. In characterization, the particle size distribution is observed not only a large size of 100 nm to 2 μm, but also a small size of 0.4-5.0 nm. The absorbance peaks of the nanocomposites exhibit a small blue shift in comparison with ZnO. The examination of morphological images explores the presence of surface defects including irregular shapes, rough surfaces, and aggregation. The nanocomposites show hexagonal wurtzite structures similar to pure ZnO. However, the nano-composites have more crystal defects than ZnO according to the $ZnFe_2O_4$ peak in XRD result and defect

peak in Raman result. Although the presence of zinc ferrite ($ZnFe_2O_4$) is also detected, magnetic hysteresis is disappeared because of poor $ZnFe_2O_4$ distribution and critical size effects. In antibacterial test, the nanocomposites were applied to inhibit the growth of *Xanthomonas campestris*, *Pseudomonas aeruginosa*, and *Pseudomonas fluorescens*. It is found that the nanocomposites can enhance antibacterial performance. From analysis, it is believed that surface and crystal defects are possible to increase interfacial contacts and accelerate antibacterial activities for the antibacterial enhancement. These findings suggest that the Fe-Cu-ZnO nanocomposites can be applied as an alternative antibacterial material.

5. Acknowledgements

This work was supported by the Department of Physics, Faculty of Liberal Arts and Science, Kasetsart University Kamphaeng Saen Campus. The authors would like to acknowledge the Kasetsart University Research and Development Institute (KURDI), Kasetsart University for English correction.

References

[1] M. J. Hajipour, K. M. Fromm, A. Akbar Ashkarran, D. Jimenez de Aberasturi, I. R. d. Larramendi, T. Rojo, V. Serpooshan, W. J. Parak, and M. Mahmoudi, "Antibacterial properties of nanoparticles," *Trends in Biotechnology*, vol. 30, pp. 499-511, 2012.

[2] S. Kim, C. Park, K.-H. Cheon, H.-D. Jung, J. Song, H.-E. Kim, and T.-S. Jang, "Antibacterial and bioactive properties of stabilized silver on titanium with a nanostructured surface for dental applications," *Applied Surface Science*, vol. 451, pp. 232-240, 2018.

[3] J. H. Hsieh, C. H. Chiu, C. Li, W. Wu, and S. Y. Chang, "Development of anti-wear and anti-bacterial TaN-(Ag,Cu) thin films-a review," *Surface and Coatings Technology*, vol. 233, pp. 159-168, 2013.

[4] C. D. Tran, J. Makuvaza, E. Munson, and B. Bennett, "Biocompatible Copper Oxide Nanoparticle Nanocomposites from Cellulose and Chitosan: Facile Synthesis, Unique Structure, and Antimicrobial Activity," *ACS Applied Materials & Interfaces*, vol. 9, pp. 42503-42515, 2017.

[5] S. Mitra, S. Chandra, D. Laha, P. Patra, N. Debnath, A. Pramanik, P. Pramanik, and A. Goswami, "Unique chemical grafting of carbon nanoparticle on fabricated ZnO nanorod: Antibacterial and bioimaging property," *Materials Research Bulletin*, vol. 47, pp. 586-594, 2012.

[6] S. Qian and Y. F. Cheng, "Fabrication of micro/nanostructured superhydrophobic ZnO-alkylamine nanocomposite films on steel for high-performance self-cleaning and anti-adhesion of bacteria," *Colloids and Surfaces A*, vol. 544, pp. 35-43, 2018.

[7] S. Wongrerkdee, S. Moungsrijun, S. Sujinnapram, S. Krobthong, and S. Choopun, "Linkage modification of a zinc oxide photoelectrode prepared with polyethylene glycol for electron transport improvement in dye-sensitized solar cells," *Bulletin of Materials Science*, vol. 42, pp. 9. 2019.

[8] R. Bomila, S. Srinivasan, S. Gunasekaran, and A. Manikandan, "Enhanced Photocatalytic Degradation of Methylene Blue Dye, Opto-magnetic and Antibacterial Behaviour of Pure and La-doped ZnO Nanoparticles," *Journal of Superconductivity and Novel Magnetism*, vol. 31, pp. 855-864, 2018.

[9] R. Bomila, S. Srinivasan, A. Venkatesan, B. Bharath, and K. Perinbam, "Structural, optical and antibacterial activity studies of Ce-doped ZnO nanoparticles prepared by wet-chemical method," *Materials Research Innovations*, vol. 22, pp. 379-386, 2018.

[10] T. K. Pathak, R. E. Kroon, V. Craciun, M. Popa, M. C. Chifiriuc, and H. C. Swart, "Influence of Ag, Au and Pd noble metals doping on structural, optical and antimicrobial properties of zinc oxide and titanium dioxide nanomaterials," *Heliyon*, vol. 5, pp. 01333, 2019.

[11] B. Ghasemi, G. Sanjarani, Z. Sanjarani, and H. Majidiani, "Evaluation of anti-bacterial effects of some novel thiazole and imidazole derivatives against some pathogenic bacteria," *Iranian Journal of Microbiology*, vol. 7, pp. 281-286, 2015.

[12] K. Niranjan, S. Dutta, S. Varghese, A. K. Ray, and H.C. Barshilia, "Role of defects in one-step synthesis of Cu-doped ZnO nanocoatings by electrodeposition method with enhanced magnetic and electrical properties," *Applied Physics A*, vol. 123, pp. 250, 2017.

[13] A. Modwi, "Fe-Cu-ZnO nanocomposite as novel adsorbent: characterizations and indigo carmine dye removal," *Journal of Optoelectronic and Biomedical Materials*, vol. 10, pp. 55-61, 2018.

[14] D. Selloum, A. Henni, A. Karar, A. Tabchouche, N. Harfouche, O. Bacha, S. Tingry, and F. Rosei, "Effects of Fe concentration on properties of ZnO nanostructures and their application to photocurrent generation," *Solid State Sciences*, vol. 92, pp. 76-80, 2019.

[15] T. K. Jana, S. K. Jana, A. Kumar, K. De, R. Maiti, A. K. Mandal, T. Chatterjee, B. K. Chatterjee, P. Chakrabarti, and K. Chatterjee, "The antibacterial and anticancer properties of zinc oxide coated iron oxide nanotextured nanocomposites," *Colloids and Surfaces B*, vol. 177, pp. 512-519, 2019.

[16] S. Bourrioux, L. P. Wang, Y. Rousseau, P. Simon, A. Habert, Y. Leconte, M. T. Sougrati, L. Stievano, L. Monconduit, Z. J. Xu, M. Srinivasan, and A. Pasturel, "Evaluation of electrochemical performances of $ZnFe_2O_4$/γ-Fe_2O_3 nanoparticles prepared by laser pyrolysis," *New Journal of Chemistry*, vol. 41, pp. 9236-9243, 2017.

[17] M. A. Ciciliati, M. F. Silva, D. M. Fernandes, M. A. C. de Melo, A. A. W. Hechenleitner, and E. A. G. Pineda, "Fe-doped ZnO nanoparticles: Synthesis by a modified sol-gel method and characterization," *Materials Letters*, vol. 159, pp. 84-86, 2015.

[18] C. B. Simões Valentin, R. L. de Sousa e Silva, P. Banerjee, and A. Franco, "Investigation of Fe-doped room temperature dilute magnetic ZnO semiconductors," *Materials Science in Semiconductor Processing*, vol. 96, pp. 122-126, 2019.

[19] S. Patra, D. Verma, A. K. Kole, C. S. Tiwary, D. Kundu, S. Chaudhuri, and P. Kumbhakar, "Optical, structural properties and antibacterial activities of uncapped and HMT capped ZnO nanoparticles," *Materials Today Communications*, vol. 12, pp. 133-145, 2017.

[20] T. Srinivasulu, K. Saritha, and K. T. R. Reddy, "Synthesis and characterization of Fe-doped ZnO thin films deposited by chemical spray pyrolysis," *Modern Electronic Materials*, vol. 3, pp. 76-85, 2017.

[21] Y. Wang, J. Hao, G. Gong, R. Chen, and Y. Su, "Effects of atmosphere and Cu doping on the magnetic properties of ZnO powders," *Physica B*, vol. 564, pp. 22-27, 2019.

[22] L. Roza, V. Fauzia, and M. Y. A. Rahman, "Tailoring the active surface sites of ZnO nanorods on the glass substrate for photocatalytic activity enhancement," *Surfaces and Interfaces*, vol. 15, pp. 117-124, 2019.

[23] Y. Wang, W. Tang, and L. Zhang, "Crystalline Size Effects on Texture Coefficient, Electrical and Optical Properties of Sputter-deposited Ga-doped ZnO Thin Films," *Journal of Materials Science and Technology*, vol. 31, pp. 175-181, 2015

[24] M. I. Khan, K. A. Bhatti, R. Qindeel, N. Alonizan, and H.S. Althobaiti, "Characterizations of multilayer ZnO thin films deposited by sol-gel spin coating technique," *Results in Physics*, vol. 7, pp. 651-655, 2017.

[25] T. Xie, L. Xu, C. Liu, and Y. Wang, "Magnetic composite $ZnFe_2O_4/SrFe_{12}O_{19}$: Preparation, characterization, and photocatalytic activity under visible light," *Applied Surface Science*, vol. 273, pp. 684, 2013

[26] J. Liu, M. Zeng, and R. Yu, "Surfactant-free synthesis of octahedral $ZnO/ZnFe_2O_4$ hetero-structure with ultrahigh and selective adsorption capacity of malachite green," *Scientific Reports*, vol. 6, pp. 25074, 2016.

[27] P. Nagaraju, Y. Vijayakumar, M. V. R. Reddy, and U. P. Deshpande, "Effect of vanadium pentaoxide concentration in ZnO/V_2O_5 nano-structured nanocomposite thin films for toluene detection," *RSC Advances*, vol. 9, pp. 16515-16524, 2019

[28] Q. Li, C. W. Kartikowati, S. Horie, T. Ogi, T. Iwaki, and K. Okuyama, "Correlation between particle size/domain structure and magnetic properties of highly crystalline Fe_3O_4 nano-particles," *Scientific Reports*, vol. 7, pp. 9894, 2017.

[29] M. Mozaffari and H. Masoudi, "Zinc Ferrite Nanoparticles: New Preparation Method and Magnetic Properties," *Journal of Superconductivity and Novel Magnetism*, vol. 27, pp. 2563-2567, 2014.

[30] M. Raghasudha, D. Ravinder, and P. Veerasomaiah, "Magnetic properties of Cr-substituted Co-ferrite nanoparticles synthesized by citrate-gel auto-combustion method," *Journal of Nanostructure in Chemistry*, vol. 3, pp. 63, 2013.

[31] R. Kumar, A. Umar, G. Kumar, and H. S. Nalwa, "Antimicrobial properties of ZnO nanomaterials: A review," *Ceramics International*, vol. 43, pp. 3940-3961, 2017.

[32] J. Redfern and M. C. Enright, "Further understanding of *Pseudomonas aeruginosa*'s ability to horizontally acquire virulence: possible intervention strategies," *Expert Review of Anti-infective Therapy*, vol. 18, pp. 539-549, 2020.

[33] Y. Hilliam, S. Kaye, and C. Winstanley, "*Pseudomonas aeruginosa* and microbial keratitis," *Journal of Medical Microbiology*, vol. 69, pp. 3-13, 2020

[34] L. Yin, D. Zhang, J. Wang, J. Huang, X. Kong, J. Fang, and F. Zhang, "Improving sunlight-driven photocatalytic activity of ZnO nano-structures upon decoration with Fe(III) cocatalyst," *Materials Characterization*, vol. 127, pp. 179-184, 2017.

[35] O. Jongprateep, N. Sato, R. Techapiesancharoenkij, K. Surawathanawises, P. Siwayaprahm, and P. Watthanarat, "Photocatalytic and antimicrobial activities of $Sr_xCa_{(1-x)}TiO_3$ (x=0, 0.25, 0.5, 0.75 and 1) powders synthesized by solution combustion technique," *Journal of Metals, Materials and Minerals*, vol. 29, pp. 42-47, 2019.